Title
Geochemical Exports to River From the Intrameander Hyporheic Zone Under Transient Hydrologic Conditions: East River Mountainous Watershed, Colorado

Journal
Water Resources Research, 54(10)

ISSN
0043-1397

Authors
Dwivedi, Dipankar
Steefel, Carl I
Arora, Bhavna
et al.

Publication Date
2018-10-01

DOI
10.1029/2018wr023377

Peer reviewed

Water Resources Research

RESEARCH ARTICLE
10.1029/2018WR023377

Geochemical Exports to River From the Intrameander Hyporheic Zone Under Transient Hydrologic Conditions: East River Mountainous Watershed, Colorado

Dipankar Dwivedi[1], Carl I. Steefel[1], Bhavna Arora[1], Michelle Newcomer[1], J. David Moulton[2], Baptiste Dafflon[1], Boris Faybishenko[1], Patricia Fox[1], Peter Nico[1], Nicolas Spycher[1], Rosemary Carroll[3], and Kenneth H. Williams[1]

[1]Earth and Environmental Sciences Area, Geochemistry Department, Lawrence Berkeley National Laboratory, Berkeley, CA, USA, [2]Applied Mathematics and Plasma Physics, Los Alamos National Laboratory, Los Alamos, NM, USA, [3]Division of Hydrologic Sciences, The Desert Research Institute, Reno, NV, USA

Key Points:
- Intrameander hyporheic zones display distinct anoxic and suboxic regions, suboxic regions being localized along sides of the meander bend
- Microtopographic features such as gullies show outsized impacts on redox processes in the hyporheic zone
- Permeability has a greater impact on biogeochemical zonation compared to the reaction pathways for transient hydrologic conditions

Supporting Information:
- Supporting Information S1

Correspondence to:
D. Dwivedi,
ddwivedi@lbl.gov

Citation:
Dwivedi, D., Steefel, C. I., Arora, B., Newcomer, M., David Moulton, J., Dafflon, B., et al. (2018). Geochemical exports to river from the intrameander hyporheic zone under transient hydrologic conditions: East River Mountainous Watershed, Colorado. *Water Resources Research*, *54*, 8456–8477. https://doi.org/10.1029/2018WR023377

Received 6 DEC 2017
Accepted 24 SEP 2018
Accepted article online 4 OCT 2018
Published online 30 OCT 2018

Abstract To understand how redox processes influence carbon, nitrogen, and iron cycling within the intrameander hyporheic zone, we developed a biotic and abiotic reaction network and incorporated it into the reactive transport simulator PFLOTRAN. Two-dimensional reactive flow and transport simulations were performed (1) to evaluate how transient hydrological conditions control the lateral redox zonation within an intrameander region of the East River in Colorado and (2) to quantify the impact of a single meander on subsurface exports of carbon and other geochemical species to the river. The meander's overall contribution to the river was quantified by integrating geochemical outfluxes along the outside of the meander bend. The model was able to capture the field-observed trends of dissolved oxygen, nitrate, iron, pH, and total inorganic carbon along a 2-D transect. Consistent with field observations, simulated dissolved oxygen and nitrate decreased along the intrameander flow paths while iron (Fe^{2+}) concentration increased. The simulation results further demonstrated that the reductive potential of the lateral redox zonation was controlled by groundwater velocities resulting from river stage fluctuations, with low-water conditions promoting reducing conditions. The sensitivity analysis results showed that permeability had a more significant impact on biogeochemical zonation compared to the reaction pathways under transient hydrologic conditions. The simulation results further indicated that the meander acted as a sink for organic and inorganic carbon as well as iron during the extended baseflow and high-water conditions; however, these geochemical species were released into the river during the falling limb of the hydrograph.

Plain Language Summary Hyporheic zones perform important ecological functions by linking terrestrial and aquatic systems within watersheds. Hyporheic zones can act as a source or sink for various metals and nutrients. Transient hydrologic conditions alter redox conditions within an intrameander hyporheic zone thus affecting the behavior of redox-sensitive species. Here we investigate how transient hydrological conditions control the lateral redox zonation within an intrameander region of the East River and examine the contribution of a single meander on subsurface exports of carbon, iron, and other geochemical species to the river. The simulation results show that exports of carbon and iron are primarily hydrologically driven, yet depend upon intermittent oxic and reductive conditions resulting from river stage fluctuations. In addition, the net exports of different geochemical species increase as the river stage decreases. This study demonstrates the importance of including hydrologic transients, using a modern reactive transport approach, to quantify exports within the intrameander hyporheic zone at the riverine scale.

1. Introduction

Hyporheic exchange refers to the bidirectional exchange of mass, energy, and living organisms between rivers and shallow subsurface waters (Briggs et al., 2014; Gomez et al., 2012). In particular, hyporheic exchange results in the interaction of nutrient-rich groundwater and oxygen-rich river water, which may lead to the formation of distinct redox gradients. These redox gradients can significantly impact the export of metals and nutrients at the local, reach, and watershed scales. However, different types of biogeochemical transformation may occur in hyporheic zones depending on their specific geomorphic, hydrological, and

biogeochemical characteristics. For example, hyporheic zone sediments of the Rookhope Burn catchment in northern England, UK, represent a diffuse source of lead contamination to streams as a consequence of past mining activities (Palumbo-Roe et al., 2012). In contrast, Harvey and Fuller (1998) demonstrated that the hyporheic zone can remove up to 20% metals like manganese through microbially enhanced oxidation at the mining-impacted Pinal Creek in Arizona. In general, our understanding of biogeochemical implications of the hyporheic exchange remains limited, particularly due to the lack of our ability to quantify how small-scale hydrological and biogeochemical processes interact and translate into measurable changes in stream ecosystems at the larger scale.

At the meander scale, various geomorphological characteristics, including sinuosity, topography, bars, pool-riffle sequences, and bed forms, can influence hydrological and biogeochemical processes (Brosofske et al., 1997; Naiman & Decamps, 1997; Stonedahl et al., 2010; Tonina & Buffington, 2007). These processes can alter the residence time of chemical species in the hyporheic zone, thereby influencing the biogeochemical processes (Boano et al., 2010; Schindler & Krabbenhoft, 1998; Zarnetske et al., 2011). In the past decade, several studies have been conducted to investigate the links between the rates of biogeochemical transformations and river morphology using the residence time concept, albeit mostly under steady state conditions (e.g., Bardini et al., 2012; Boano et al., 2010; Marzadri et al., 2010). Dynamic stream-aquifer interaction is recognized in the literature as having significant implications for stream water chemistry and the hyporheic exchange (Arora, Dwivedi, et al., 2016; Arora, Spycher, et al., 2016; Boano et al., 2008; Cardenas, 2007; Dwivedi et al., 2017, 2018; Siergieiev et al., 2015). However, only limited studies have addressed biogeochemical processes under transient conditions, and these studies have been primarily restricted to quantifying nitrate production and the removal or *representative* solutes of nitrate cycling within the hyporheic zone. Briggs et al. (2014), for example, indicated that transient nitrate dynamics in the hyporheic zone were primarily driven by changes in physical hydrology through bed forms and associated residence times. Similarly, Zarnetske et al. (2011) used residence times to examine nitrogen-cycling dynamics in the hyporheic zone, while Gu et al. (2007) used the Damköhler number concept. Although it is well established that sinuosity-driven hyporheic exchange affects the biogeochemical transformation across the redox ladder, only a few studies have addressed or accounted for biotic and abiotic interactions, and in most cases with idealized representations (e.g., Boano et al., 2006; Cardenas, 2009; Revelli et al., 2008). Although informative, these previous studies have not evaluated the cumulative effect of chemical reactions within the intrameander hyporheic zone of a single meander on downstream chemistry under transient conditions.

Redox-sensitive species within the intrameander hyporheic zone are influenced by transient hydrologic conditions, such as groundwater flow dynamics, river stage fluctuations, and rainfall/snowmelt events. For example, Arora, Spycher, et al. (2016) suggested that the temporal behavior of redox-sensitive species (e.g., uranium, vanadium) was associated with seasonal hydrologic variability—rainfall and snowfall events—at a contaminated floodplain site in Rifle, Colorado. Furthermore, many studies have linked the migration and distribution of contaminants away from the groundwater-surface water interface to hydrological transients (e.g., Arora et al., 2013; Cozzarelli et al., 2011; Dwivedi & Mohanty, 2016; Dwivedi et al., 2016; Yabusaki et al., 2017). Because of the complexity of biogeochemical processes and the likelihood that they will show a variable response during the wetting of soils and oxic conditions, transient hydrological conditions may alter the behavior of nutrients and metals within the intrameander hyporheic zone and consequently affect the chemical signature of rivers at the larger scale.

Although previous studies have targeted rigorous theoretical modeling of morphological characteristics of the meander, here we use high-resolution hydrodynamic assessments of the hyporheic zone combined with detailed pore water sampling to focus on the hyporheic exchange at the meander scale and to quantify the subsurface exports from a single meander to the river under transient hydrological conditions. Specifically, we aim to capture the effect of river stage variations on hydrologic and geochemical behavior within and exports from the intrameander hyporheic zone. The overall objectives of the study are to (1) examine how transient hydrological conditions (e.g., river stage variations, rainfall events) control the lateral redox zonation within the intrameander hyporheic zone, (2) perform a sensitivity analysis to identify the key physical and geochemical parameters controlling lateral redox zonation; and (3) quantify the cumulative effect of chemical reactions in intrameander hyporheic zones on the subsurface exports of carbon and iron into the river.

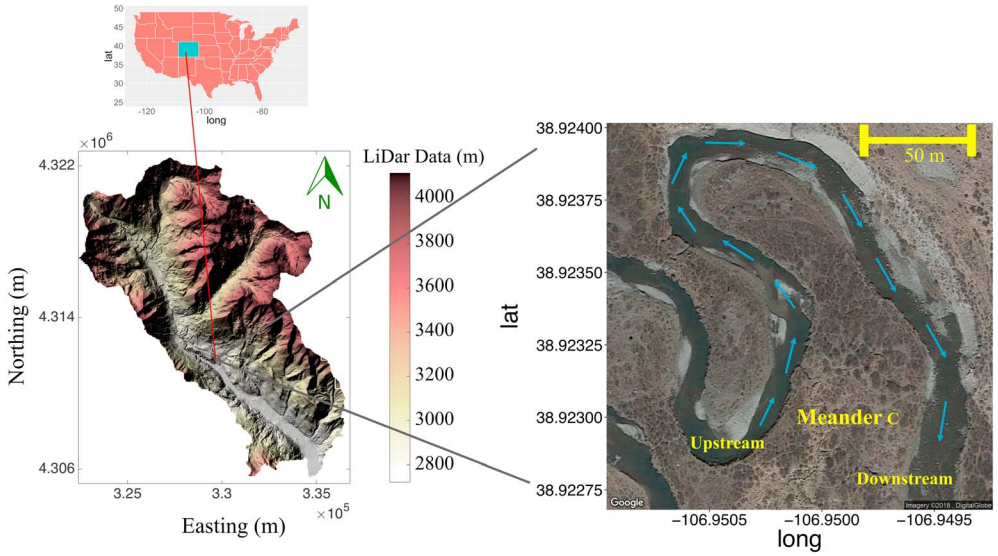

Figure 1. Location of the East River floodplain and meander C study site in Colorado. Blue arrows show the flow direction in the river.

This paper is organized as follows. First, a brief overview of the field site and data sets is presented. Next, we describe our flow and reactive transport model that considers aqueous speciation, microbially mediated redox reactions, and precipitation/dissolution of minerals representative of the meander system at the East River. Then, we describe the lateral redox zonation and the impact of transient hydrologic conditions on biogeochemical character of the intrameander hyporheic zone of the East River. Finally, we quantify the overall contribution of the meander to the river by integrating geochemical out-fluxes along the outside of the meander bend.

2. Field Site and Data Sets

2.1. Site Characteristics

We conducted this modeling study in the East River floodplain, located in a high-elevation catchment in southwestern Colorado (between 38.8° to 38.9° and 106.8° to 106.9°W) with rolling-to-mountainous topography. The floodplain includes multiple river meanders that extend over a distance of 11 km (Figure 1). The East River floodplain demonstrates distinctive fluvial progression and is representative of other headwater systems within the upper Colorado River basin. The site encompasses the drainages of the East River and Copper Creek; the stream flow is fed predominantly by snowmelt in late spring to early summer, with middle to late-summer monsoonal rainfall triggering rapid but punctuated increases in flow (Hubbard et al., 2018; Markstrom et al., 2012; Winnick et al., 2017). The area experiences an average temperature ranging from a low of −8 °C in January to a high of 35 °C in July.

The geology of the watershed is marked by a diverse suite of Paleozoic and Mesozoic sedimentary rocks intruded by Tertiary igneous laccoliths and ore-rich stocks. The site consists of Cretaceous Mancos Shale bedrock overlain by glacial moraine deposits (Gaskill et al., 1991). The Mancos Shale formation is an agglomeration sequence of heterogeneous marine black shale with regions of elevated metal, metalloid, and pyrite content (Kenwell et al., 2016; Morrison et al., 2012). The major reactive minerals identified at the site in river sediments are calcite, ferrihydrite, and pyrite found in core samples collected from boreholes 1–1.10-m deep below the surface, near the Meander C Piezometric (MCP) transect (Figure 2; MCP transect described in section 2.2).

The watershed is underlain by an unconfined alluvial aquifer that is hydrologically connected to the East River and to the meander investigated in this study, a conclusion that was confirmed based on piezometric head measurements. The interactions between the floodplain aquifer and East River meanders lead to

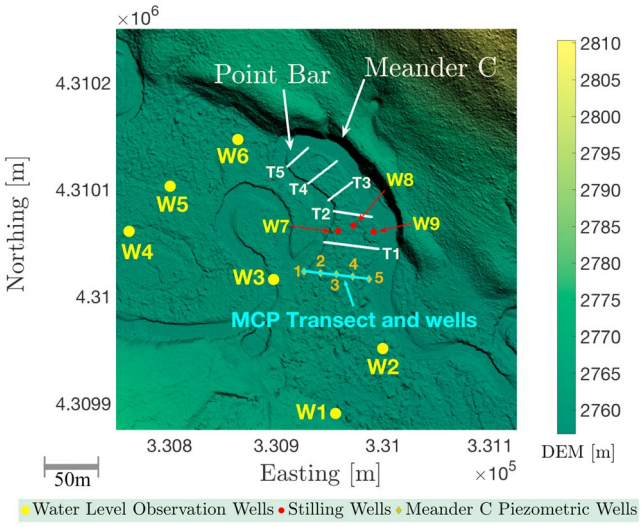

Figure 2. The MCP transect that was modeled in this study is located within the intra-meander hyporheic zone. River meander topography is based on 0.5-m resolution Light Detection and Ranging data. The MCP transect includes five piezometric observation wells (MCP1 to MCP5) for geochemical samples. Six observation wells (W1 to W6) were used to monitor water levels using pressure transducers. Three additional stilling wells (W7 to W9) were used to project river stage on the downstream side (near well MCP5) of the river. Equispaced transects (T1 to T5), perpendicular to the meander neck toward the point bar, were modeled to compute the overall biogeochemical contribution of the meander to the river.

various potential hyporheic flow paths; the investigation of these flow paths within an intrameander region at the East River is the subject of this study.

2.2. Hyporheic Zone Data

Because of the spatial heterogeneity inherent in a floodplain environment, we model a well-instrumented transect of meander C of the East River site (two-dimensional *x-z* model domain) that is approximately parallel to the hyporheic flow field, labeled as MCP on Figure 2. Specifically, the MCP transect includes five piezometric observation wells for geochemical samples (Wells MCP1 to MCP5), and these wells and transect are accordingly referred to as MCP wells and MCP transect (Figure 2). Stainless steel drive-point piezometers (Model 615; Solinst Canada, Ltd.) were installed to achieve a sampling depth of 1.85 m below ground surface. Each piezometer consisted of a stainless-steel sampling drive-point body with a cylindrical filter screen (50 mesh) connected to a suitable length of polyethylene tubing from which groundwater samples were obtained using a peristaltic pump. In addition, six observation wells (W1 to W6), close to the MCP transect, were used to monitor water levels using pressure transducers. Precipitation data were obtained from the Weather Underground station KCOMCRET2 located on Mount Crested Butte, Colorado (website: https://www.wunderground.com/personal-weatherstation/).

Geochemical samples were collected from MCP1 to MCP5 and river water in July (before and after rain) and August 2016, during intermittent rain events. Groundwater was pumped from each piezometer using a peristaltic pump and sampled after purging a volume of water equivalent to 3 times the water standing in each piezometer. Unfiltered groundwater samples were collected for pH, electrical conductivity (EC), oxidation-reduction potential (ORP), and dissolved oxygen in the field, and filtered (0.45 m PVDF syringe filters) samples were collected for in-field iron (II) (Fe^{2+}) measurement and laboratory analysis of metals and dissolved organic and inorganic carbon. Dissolved oxygen (DO), nitrate (NO_3^-), and Fe^{2+} were measured colorimetrically in the field using a portable spectrophotometer and CHEMetrics vacuvials (chemets). DO was measured either with the indigo carmine method (#K-7513, 1–15 ppm) or the Rhodazine D™ method (#K-7553, 0–1 ppm), with accuracy ranging from ±0.6 to ±1.1 ppm and ±0.025 to ±0.080 ppm, respectively. Nitrate was measured using the cadmium reduction method (#K-6903, 0–1.5 ppm) with accuracy ranging from ±0.10 to ±0.33 ppm. Fe^{2+} was measured using the phenanthroline method (#K-6203, 0–6 ppm) with accuracy ranging from ±0.08 to ±0.045 ppm (https://www.chemetrics.com/). A multiparameter probe was used for pH, EC, and ORP measurements. Groundwater samples were analyzed for total dissolved carbon and dissolved organic carbon (DOC) on a Shimadzu TOC-V analyzer with a nondispersive infrared detector, and dissolved inorganic carbon was determined by the difference. Total dissolved carbon was measured by catalytically aided combustion at 680 °C, and DOC samples were analyzed by nonpurgeable organic carbon, for which samples were acidified with HCl and purged with N_2 in order to remove inorganic carbon prior to the analysis. Metal concentrations were measured by ICP-MS (Perkin-Elmer Elan DRC II) after acidification and dilution with ultrapure 0.16 M nitric acid and internal standard addition.

Sediments were collected within 60 cm of each MCP piezometer at approximately 15-cm depth intervals using either a 2-inch (5-cm) diameter slide hammer corer or bucket auger. At the end of each sampling day, sediments were sealed into Mylar bags with oxygen absorbers in order to maintain an anaerobic environment and stored at 4 °C. Samples were then shipped (cold) to the laboratory and each core section was homogenized and sieved through a 2-mm sieve under field moist conditions. A subsample of the <2-mm fraction was air-dried at room temperature and ball-milled using tungsten-carbide balls to a fine powder. Total free iron oxide content (CBD-Fe) was determined by extracting finely ground sediment with 0.3 M sodium citrate, 0.1 M sodium bicarbonate, and sodium dithionite at 80 °C on duplicate samples (Loeppert & Inskeep, 1996). Sediment samples were also analyzed for total carbon (TC) by catalytically aided

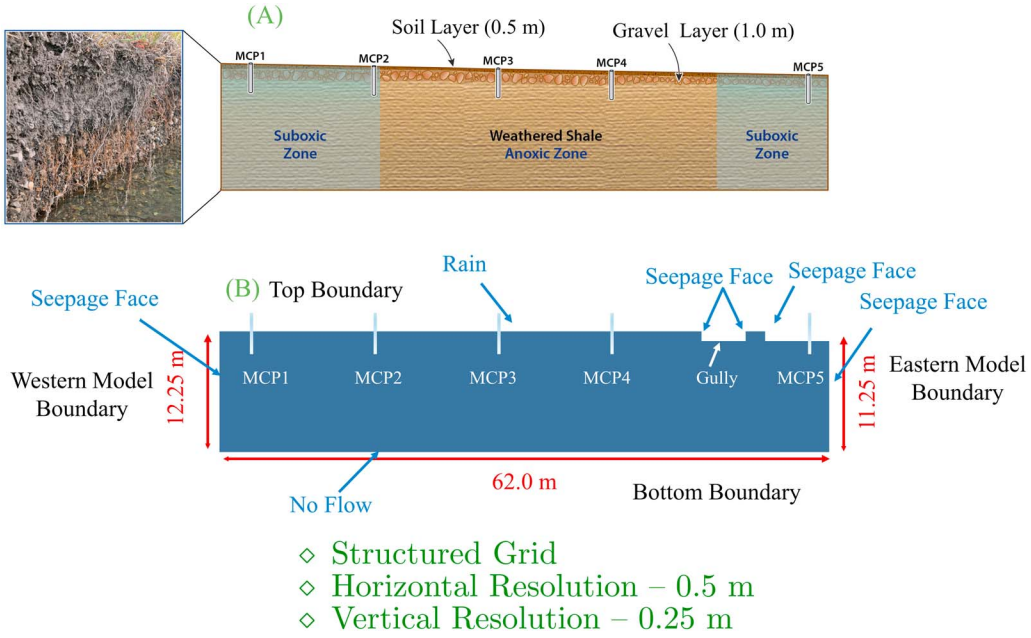

Figure 3. (a) Geological description of the modeled MCP transect; (b) modeling domain including boundary conditions and well locations along the MCP transect. The western and eastern boundaries are on the upstream and downstream sides of the MCP transect, respectively. The NAVD88 elevation of the bottom boundary of the model is 2748 m.

combustion oxidation at 900 °C and a NDIR detector using a Shimadzu TOC-V analyzer equipped with a solids module (SSM) on ball-milled sediments. Air-dried sediment was ball-milled using tungsten-carbide balls to a fine powder. Total inorganic carbon (TIC) analysis was performed by acidification of samples with 20% phosphoric acid and heated to 200 °C in a Shimadzu TOC-V analyzer and the evolved CO_2 was measured. Total organic carbon was determined by difference between TC and TIC.

3. Biogeochemical Reactive Transport Model

The model was structured as a two-dimensional *x-z* model representing hyporheic flow paths as well as hydrological and biogeochemical processes between the East River and the underlying aquifer along the modeled transects (Figure 2). Several model simulations were run using PFLOTRAN, which is an open source, three-dimensional, reactive flow and transport simulator (Hammond et al., 2014). The simulations were mainly divided into three sets: (a) a baseline simulation corresponding to the MCP transect; (b) simulations for performing sensitivity analyses to identify the key physical and geochemical parameters of the baseline simulation; and (c) simulations capturing the cumulative exports from a single meander system to the river. A detailed description of the different simulations is provided in section 3.5.

3.1. Model Domain and Discretization

In this study, the MCP transect model consisted of three hydrostratigraphic layers that were based on field investigations of the site (Figure 3a). The top hydrostratigraphic unit was a relatively low permeability (8.8×10^{-14} m^2) soil layer that was underlain by a high-permeability (2.26×10^{-11} m^2) gravel layer. The bottom-most hydrostratigraphic unit consisted of a low permeability (8.3×10^{-15} m^2) weathered shale layer.

The modeling domain consisted of a 62-m long by 12.25-m deep 2-D rectangular domain that followed one of the hyporheic flow paths within the intrameander region (Figure 3b). A structured grid of the modeling domain was created using a digital elevation model derived from a high-resolution Light Detection and Ranging data set having a spatial resolution of 0.5 m (Wainwright & Williams, 2015). The domain was discretized using 6,076 grid blocks with a uniform grid spacing of 0.5 m along the horizontal direction and 0.25 m along the vertical direction. A maximum time step of 1,800 s was used for all simulations. We also performed sensitivity analyses of redox zonation using the MCP transect model.

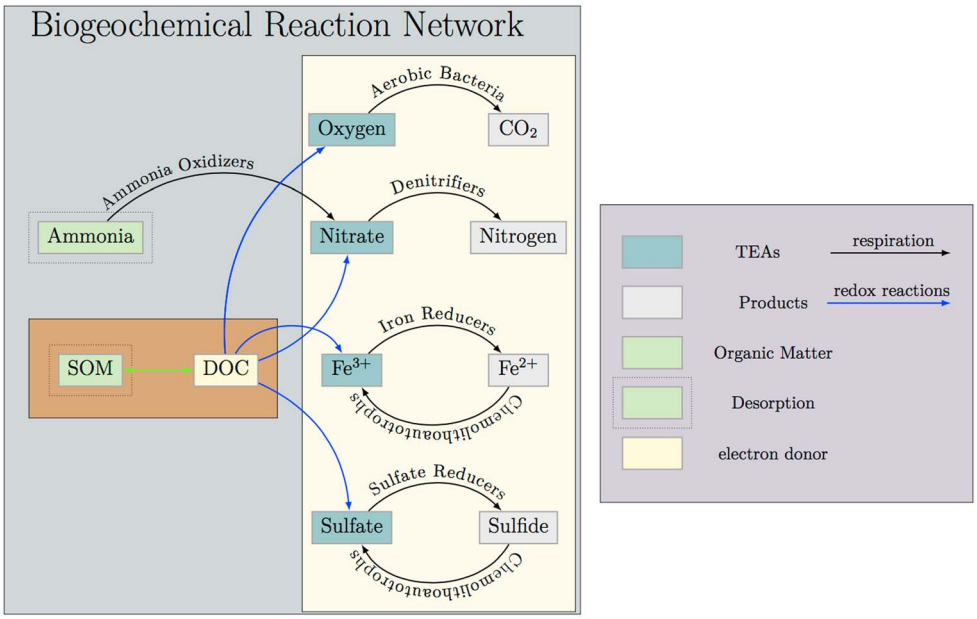

Figure 4. Schematic representation of the biogeochemical reaction network included in model simulations.

To compute the overall contribution of the meander to the river, we modeled five additional transects perpendicular to the meander neck toward the point bar (Figure 2). These transects (referred to as the T1, T2, T3, T4, and T5 transects, or T transects, collectively) included three hydrostratigraphic layers (top 0.5-m soil layer; 0.5- to 1.5-m gravel; and remaining as weathered shale) similar to the MCP transect. The domain for each transect was also discretized similar to the MCP transect with a uniform grid spacing of 0.5 m along the horizontal direction and 0.25 m along the vertical direction. For all the simulations involving *T* transects, the maximum time step was assigned as 1,800 s. The modeling extent and number of grid blocks of these transects are provided in supporting information Table S1.

3.2. Hydrological System

PFLOTRAN was used with the Richards equation (Richards, 1931) option for variably saturated flow (Hammond et al., 2014). The relationship between capillary pressure and saturation was described using the van Genuchten model. The Mualem formulation was used to relate relative permeability and van Genuchten saturation function. The average hydrological properties were estimated using pedotransfer functions from textural data of sediments from the site. These values are summarized in Table S2.

3.3. Geochemical System

To evaluate the biogeochemical implications of the hyporheic exchange resulting from the transient hydrological conditions at the meander scale and their cumulative influence at the large scale, we incorporated a biogeochemical reaction network into PFLOTRAN Figure 4, supporting information Tables S3–S6; for more information see Arora, Spycher, et al., 2016; Davidson et al., 2012; Doussan et al., 1997; Handley et al., 2013; Helgeson et al., 1978; Li et al., 2010; Luther et al., 2011; Majzlan et al., 2004; Mayer et al., 2002; Palandri & Kharaka, 2004; Palmer et al., 2010; Parkhurst & Appelo, 1999; Russell, 1973; Shock et al., 1997; SNL, 2007; Widdowson et al., 1988; Williamson & Rimstidt, 1994; Wu et al., 2011). The reaction network included the microbial consumption of dissolved organic carbon (DOC), which is produced through acetogenesis—a solid organic matter (SOM) producing dissolved organic carbon (acetate) as follows:

$$C_6H_{10}O_5 + H_2O \rightarrow \ 3CH_3COO^- + 3H^+ \quad (1)$$

The heterotrophic decomposition of DOC was represented by overall reactions for aerobic respiration, denitrification, iron reduction, and sulfate reduction. The microbial decomposition rate of substrate DOC was calculated using single Michaelis-Menten kinetic reactions using a general rate law (Table S5):

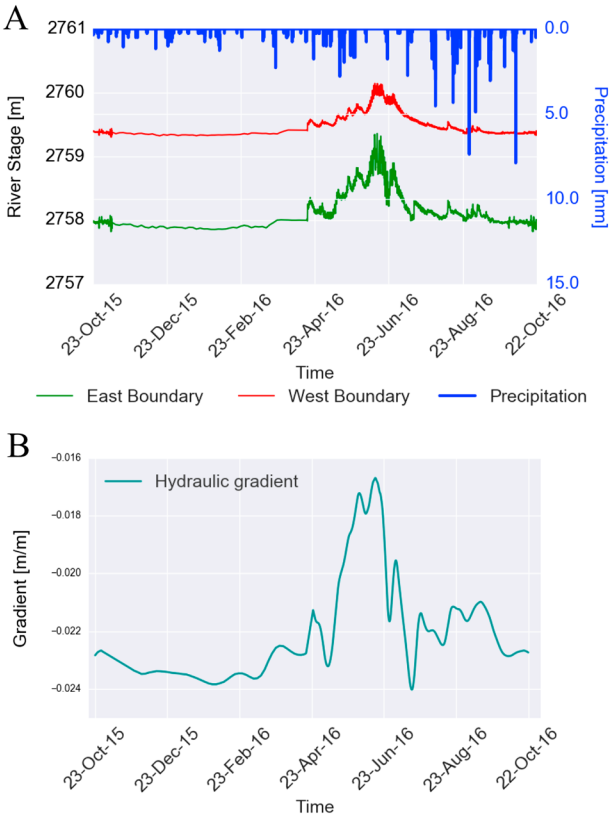

Figure 5. (a) Water levels (on the left *y* axis) at the eastern and western boundaries show that high-water conditions occur at the site starting from mid-April to June; subsequently water level decreases until October. NAVD88 datum was used for river stage data and water level elevations. Precipitation data are shown on the right *y* axis; (b) the hydraulic gradient across the two ends of the studied transect tends to be stronger when the river stage is lower.

$$R_s = \mu_{\max} \frac{C_S}{K_S + C_S} \frac{C_{\mathrm{TEA}}}{K_{\mathrm{TEA}} + C_{\mathrm{TEA}}} \frac{K_I}{K_I + C_I} \tag{2}$$

where $\mu_{\max}$ is the maximum rate of reaction, C_S is the substrate concentration, C_{TEA} is the electron acceptor concentration, and C_I is the inhibitor concentration. K_S, K_{TEA}, and K_I are the corresponding half-saturation constants for the substrate, terminal electron acceptors (TEAs), and inhibition constant, respectively. In addition to the heterotrophic reactions involving DOC, we also incorporated chemolithoautrophic oxidation of Fe^{2+} and S^{2-} to account for iron and sulfur cycling. However, we did not include dissimilatory nitrate and nitrite reduction into NH_4^+ in our reaction network, as nitrate was not prevalent in anoxic zones of our study and the dissimilatory pathway of nitrogen species usually occurs in anaerobic soils rich in nitrate (Knowles, 1982; Maggi et al., 2008). The corresponding reactions and their kinetic rate law and parameters are given in supporting information Table S6.

The reaction network included 20 primary species and 72 secondary species. The primary species included in the model were: H^+, K^+, Na^+, Ca^{2+}, Mg^{2+}, Fe^{2+}, Fe^{3+}, Al^{3+}, H_2O, acetate, O_2 (aq), SiO_2 (aq), N_2 (aq), NH_3 (aq), NO_3^-, NO_2^-, Cl^-, HCO_3^-, S^{2-}, and SO_4^{2-}. The model considered aqueous speciation at equilibrium as well as mineral precipitation and dissolution reactions at equilibrium or under kinetic constraints depending on the mineral (supporting information Table S3). The minerals considered in the model were ferrihydrite, pyrite, calcite, and SOM, the proxy *mineral* used for solid organic matter (reaction (1)). Kinetic mineral precipitation and dissolution were modeled using transition state theory (TST)-type rate laws:

$$R_m = \left(k_{25}^{n} + k_{25}^{\mathrm{ac}}[a_{H^+}] + \Sigma k_{25}^{\mathrm{ex}} \Pi_i [a_{ij}]\right)(1 - \mathrm{Q}_m/\mathrm{Keq}_m) \tag{3}$$

where k_{25}^{n}, k_{25}^{ac}, and k_{25}^{ex} represent rate constants for neutral, acid, and additional (*j*th) reaction mechanisms at 25 °C, respectively; a_{ij} represents the activity of the *i*th aqueous species in the *j*th reaction, whereas Q_m represents the ion activity product of the m_{th} mineral phase; and *Keq* represents the corresponding equilibrium constant (see Table S4). Reaction stoichiometry and kinetic parameters associated with mineral precipitation and dissolution reactions are summarized in the supporting information Tables S3 and S4.

3.4. Initial and Boundary Conditions

A dynamic seepage face boundary condition was imposed at the eastern (downstream) and western (upstream) boundaries of the model domain by applying observed transient river stage measurements and river gradient data at these locations (Figures 3 and 5). A seepage face boundary is an interface at atmospheric pressure (P_{atm}) where the water exits the porous medium (Bear, 1972). The pressure at the boundary (P_{boundary}) is calculated as follows:

$$P_{\mathrm{boundary}} = \max(Hydrostatic, P_{\mathrm{atm}}) \tag{4}$$

Water levels at wells MCP1 to MCP5 were estimated with pressures calculated through the interpolation of inland well head data measured at wells W1 to W6 (Figure 2). The river stage on the western boundary of the model was measured using a pressure transducer, while on the eastern boundary of the model it was computed through the interpolation of inland well head data measured at stilling wells W7 to W9 and projected onto the measured bathymetry. The hydraulic gradient was estimated using river stage elevations at the two ends of the studied transect, aligned with the flow direction (Figure 5b).

A no-flow boundary condition was imposed on the bottom boundary, which we justify on the basis of the low permeability of the underlying shale. Time-varying recharge from rain was applied as the top boundary condition (Figure 5a). The initial flow condition was a hydrostatic pressure distribution, where the water level was set at 5.0 m below the land surface (7.25 m above the model bottom boundary).

The river water composition (as opposed to groundwater) at the eastern and western model boundaries (i.e., from 0 to 2 m below the ground level) was fixed at values determined from measurements in river samples collected near wells MCP1 and MCP5 (Table S7). Although we acknowledge that the river chemistry might change at different times, geochemical samples from river water that were collected in July (before and after rain) and August 2016 showed comparable chemical compositions (see supporting information Table S8). Therefore, for simplicity, we did not consider potential variations in the river water composition as used for defining model boundary conditions.

A fixed groundwater composition (i.e., from 2 to 12.25 m, below the ground level) was also applied at the eastern and western model boundaries (Table S7). The composition was based on measurements from wells MCP1 and MCP5. The concentrations of S^{2-} and Fe^{3+} in groundwater at that location were calculated to yield equilibrium of the groundwater with pyrite and ferrihydrite, respectively. Rain water composition is provided in Table S9 that was used for recharge at the top model boundary. Initial conditions over the entire model domain were based on measurements from wells MCP1, although the initial water concentrations have little effect once more than one pore volume has been flushed through the system (Table S7). The sediments throughout the entire domain were set with an initial mineral composition, as described in Table S10. The proxy organic matter phase was given an equilibrium constant calculated to yield acetate concentrations (at equilibrium with this phase, reaction (1)) representative of measured concentrations (see Table S3). The model was run for several years to achieve dynamic equilibrium for the hydrologic and chemical conditions prior to actual simulations for an entire year (23 Oct 2015 to 22 Oct 2016) in the East River floodplain.

3.5. Model Simulations

Several reactive transport simulations were run to understand how river stage fluctuations, hydraulic gradients, reaction pathways, and permeability influence redox gradients in meanders and thus the geochemical exports to the river (Table 1). All simulations were carried out using a 2-D model setup in the hyporheic aquifer zone. The baseline simulation was run by incorporating a fully coupled biotic and abiotic biogeochemical system (Figure 4) with river stages along the eastern and western boundaries as shown in Figure 5a. We compared the baseline model simulation with data collected from the five wells along the MCP transect (MCP1 through MCP5).

The second set of simulations included eight sensitivity tests (Table 1) to explore how hydrologic and biogeochemical changes may impact redox zonation. As described in Table 1, the M1 to M4 simulations quantified how river stage variations influenced the hydrologic and biogeochemical character along the MCP transect. Simulations M5 and M6 examined how permeability values affected redox gradients (see Tables 1 and S2). Accordingly, differences between the baseline and the M5 and M6 simulations were used to examine the influence of permeability on the redox zonation. In addition, M7 and M8 simulations captured the biogeochemical system (a) without microbial reactions to quantify the relative contribution of biotic and abiotic pathways in the hyporheic zone and (b) with microbial reactions, but not involving chemolithoautotrophic pathways to isolate the effect of Fe and S cycling on the river's chemistry. Differences between the baseline and the M7 and M8 simulations were used to examine how reaction pathways impacted redox zonation.

The third set of simulations quantified the overall contribution of a single meander to the river by integrating geochemical out-fluxes along the outside of the meander bend (Figure 2). These out-fluxes were computed by running multiple 2-D simulations representing a fully coupled biotic and abiotic biogeochemical system using the *T* transects as described in section 3.1.

Except for the reaction network, the current model was not calibrated for the spatially variable material properties. The reaction network was calibrated to obtain pH in groundwater close to measured values by adjusting the kinetic rate of iron reduction. In addition, the half rate constant of iron was modified to yield background dissolved Fe^{2+} concentrations close to the measured values. The hydrologic properties and surface area were estimated based on particle size distributions, sediment properties, and geophysical data (e.g., section 2.2, Tables S2 and S10), but these properties were not spatially conditioned on 2016 field

Table 1
Description of Various Reactive Transport Simulations, Parameters, and Boundary Conditions, for Example, Western River-Stage (WRS) and Eastern River-Stage (ERS) Used in the Sensitivity Analysis

Simulation	Permeability multiplier	Heterotrophic pathways present	Chemolitho-autotrophic pathways present	Mineral reactions	River-stage fluctuations (west boundary)	River-stage fluctuations (east boundary)
Baseline	1	Yes	Yes	Yes	WRS	ERS
M1	1	Yes	Yes	Yes	Steady (mean of WRS)	Steady (mean of ERS)
M2	1	Yes	Yes	Yes	WRS	WRS multiplied with a constant gradient = −0.021
M3	1	Yes	Yes	Yes	WRS	ERS (15% higher)
M4	1	Yes	Yes	Yes	WRS	ERS (30% higher)
M5	10	Yes	Yes	Yes	WRS	ERS
M6	0.1	Yes	Yes	Yes	WRS	ERS
M7	1	No	No	Yes	WRS	ERS
M8	1	Yes	No	Yes	WRS	ERS

Note. Rows shaded in blue, green, yellow, and gray refer to the baseline simulation, hydrologic perturbations, permeability variations, and different reaction pathways, respectively.

observations. Calibrating the model on field observations would improve the match, but that was not our objective. Rather, our goal was to develop a robust modeling approach that can predict the redox environment associated with O_2, NO_3^-, and Fe^{2+} resulting from hydrologic transients.

4. Results and Discussion

4.1. Water Table Dynamics

The river stage dynamics along the western and eastern boundaries influenced the time-dependent variation in groundwater levels and hydraulic gradients along the MCP transect. The river stage fluctuated a maximum of 0.8 m, with a standard deviation of 0.18 m, at the western boundary. However, the river stage levels at the eastern boundary showed a higher variability; the fluctuation ranged up to 1.68 m, with a standard deviation of 0.30 m (Figure 5a). The highest river stage at this site occurred in mid-April to June and then decreased until October. Figure 6 shows simulated and observed water levels at wells MCP1 to MCP5 for an entire year (23 Oct 2015 to 22 Oct 2016) in the East River floodplain. Simulated water levels closely matched the observed values (R^2 values ~ 0.98), and the model captured the hydrologic variability quite well. Consistent with observations, the flow simulation results suggest that the water table generally rises by a maximum of 1.2 m, with a standard deviation of 0.27 m, in late spring to early summer. Such a rise in the water table primarily corresponds with the snow melt in the East River floodplain (Winnick et al., 2017).

Pressure contours for the four different times obtained from the baseline simulation are shown in the supporting information Figure S1. Pressure contours in October 2015 and August 2016 represent the logarithmic pressure distribution during low-water conditions, while the pressure contours in June 2016 (during peaking) and July 2016 (falling limb after peaking) represent the logarithmic pressure distribution during the high-water conditions. Pressure contours demonstrate that the flow close to the gully was driven by pressure gradients resulting from the topographic depression and low permeability in the soil layer.

Figure 7 shows water (liquid) saturation and flow velocities along the MCP transect obtained from the baseline and M4 simulations. M4 simulation represented lower hydraulic gradients in river stages across the western and eastern boundaries by 30% compared to the baseline simulation. Figure 7 shows that groundwater velocities were twice as high during periods of high-water conditions than during periods of low-water conditions for both the baseline and M4 scenarios. Despite smaller hydraulic gradients during high-water conditions, groundwater velocities were higher because the rise of the water table brought more water to flow within the gravel layer (i.e., larger saturated section within this layer). In addition, as would be expected, groundwater velocities were higher (2 to 4 times at different times) for the baseline scenario compared to the M4 simulation because of the lower hydraulic gradients in the latter case. Groundwater velocities computed by the model (in the range of 1.25×10^{-5} to 5.09×10^{-6} m/s in the top 2 m) suggested that the

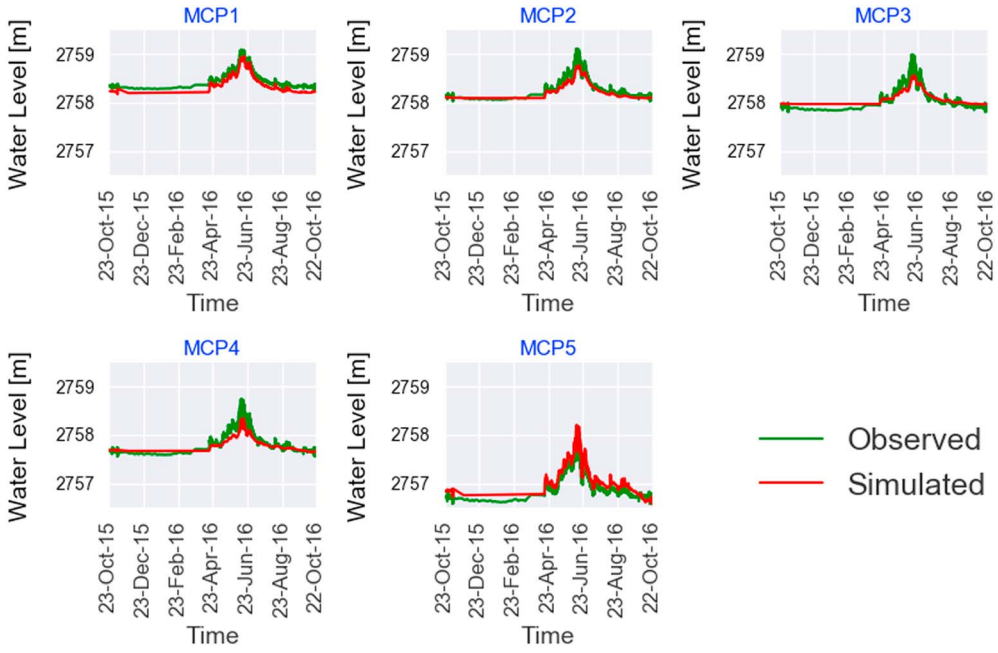

Figure 6. Observed and simulated water levels in wells MCP1 to MCP5.

residence time of groundwater along the MCP transect was on the order of 1 to 2 months. Simulations M2 and M3 also manifested similar trends and proportional changes in groundwater velocities during high- and low-water conditions (not shown here). For example, M3 resulted in higher groundwater velocities than M4 because of higher hydraulic gradients in river stages across the western and eastern boundaries. Moreover, Figure 7 shows that groundwater discharges into the gully during high-water conditions.

Figure 7 also demonstrates the extent of the vadose zone during high- and low-water conditions. It is evident that the vadose zone extended vertically more than 1 m during low-water conditions, and the extent of the vadose zone was greater for the baseline scenario than the M4 simulation, as would be expected due to the relatively lower river stage along the eastern boundary in the baseline simulation.

4.2. Chemical Zonation Along the Modeled Transect

Figure 8 shows that the simulated concentrations of DO, nitrate, Fe^{2+}, TIC, and pH compared reasonably well with the field observations along the MCP transect, with the exception of the observed lower iron

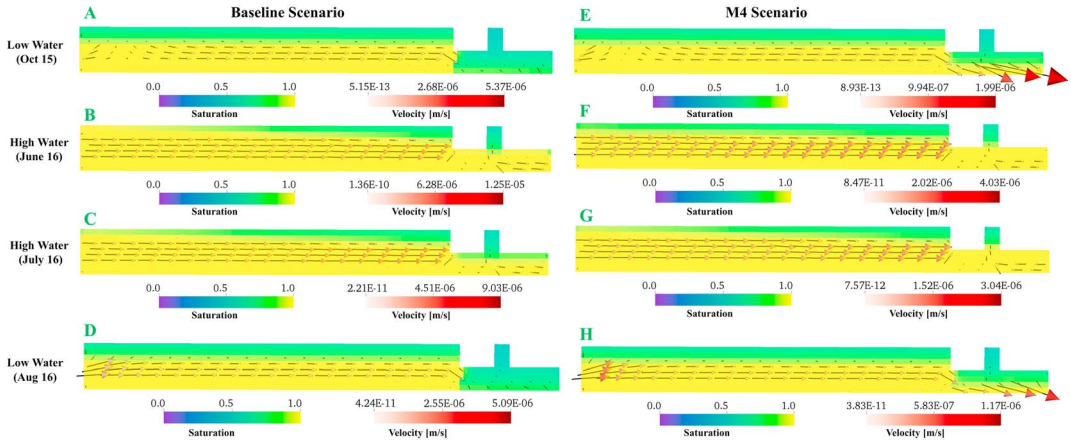

Figure 7. Water (liquid) saturation and groundwater flux velocities along the MCP transect shown in top 2.25-m depth at the western boundary and 1.25-m depth at the eastern boundary.

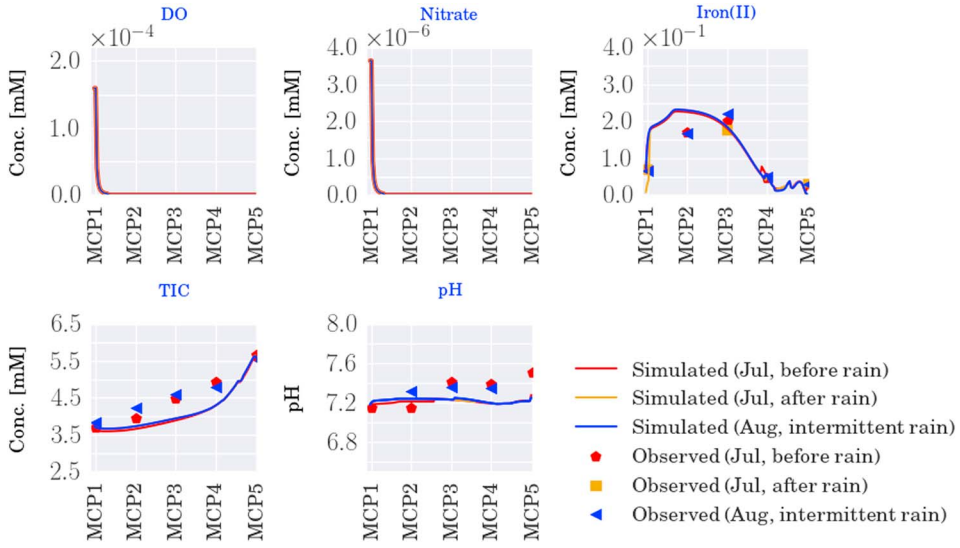

Figure 8. Observed and simulated concentrations of dissolved geochemical species in groundwater along the MCP transect.

concentrations at MCP2 (July and August) and the observed slightly higher TIC concentrations at MCP3 and MCP4 (July and August). However, the maximum differences between the predicted and observed Fe^{2+} and TIC values along the MCP transect were less than 0.15 mM and 0.66 mM, respectively. Moreover, the maximum difference between the predicted and observed values in pH was less than 0.32. In general, the model captured the trends correctly, and the minor differences between predicted and observed values in pH and geochemical species could be because of local heterogeneities resulting from various factors, such as particle size distributions and sediment properties in a field system like ours, which we did not resolve in our model. Note that observed DO and nitrate concentrations fell below the detection limit of the CHEMetrics ($<$0.8 μM for DO; and $<$7 μM for nitrate). In addition, sulfide species were insignificant along the MCP transect; therefore, we have not presented results for sulfide.

As Figure 8 suggests, the baseline model simulations showed a decline in DO and nitrate, but an increase in iron (Fe^{2+}) concentration along the modeled transect. The presence of DOC as an energy source within the intrameander sediments resulted in a gradual depletion of the available TEAs, leading to the formation of a reducing redox gradient along the MCP transect. The magnitude and length of this gradient depended on how far and how quickly oxic water entered the hyporheic zone. Initially, oxygen was consumed as the main TEA while other TEAs, such as nitrate and Fe^{3+}, were inhibited to impede the lower Gibb's free-energy biotic-redox reactions. When the oxygen concentration decreased lower than the limiting value, nitrate, iron, and sulfate were sequentially reduced (i.e., the system moves down the redox ladder). Figure 8 shows that simulated oxygen and nitrate were both completely reduced within the first meter along the flow path near well MCP1. Here groundwater did not exhibit detectable nitrate, but did show dissolved iron (Fe^{2+}), indicating that reducing conditions prevailed and Fe^{3+} from ferrihydrite was reduced to Fe^{2+} in groundwater. Because the seepage velocities were low, this short distance provided sufficient time for the biogeochemical reactions to occur. Unlike at MCP4, the presence of elevated dissolved iron at well MCP3 suggests that the groundwater along the meander centerline was isolated and was not actively receiving oxygenated recharge. In contrast, MCP4 received oxic water because the groundwater discharged into the gully during the high-water conditions, which subsequently infiltrated downward. As a result, well MCP4 showed low dissolved iron.

Figure 9 shows the spatial distribution of these geochemical species computed using model results of the *T* transects in July. The spatial distributions of different dissolved geochemical species indicated that DO and nitrate decreased quickly whereas iron first increased and then decreased along the *T* transects. In addition, TIC increased whereas pH did not show any significant variability along the *T* transects. Iron manifested the highest variability within the intrameander region of meander C. The simulation results further demonstrate

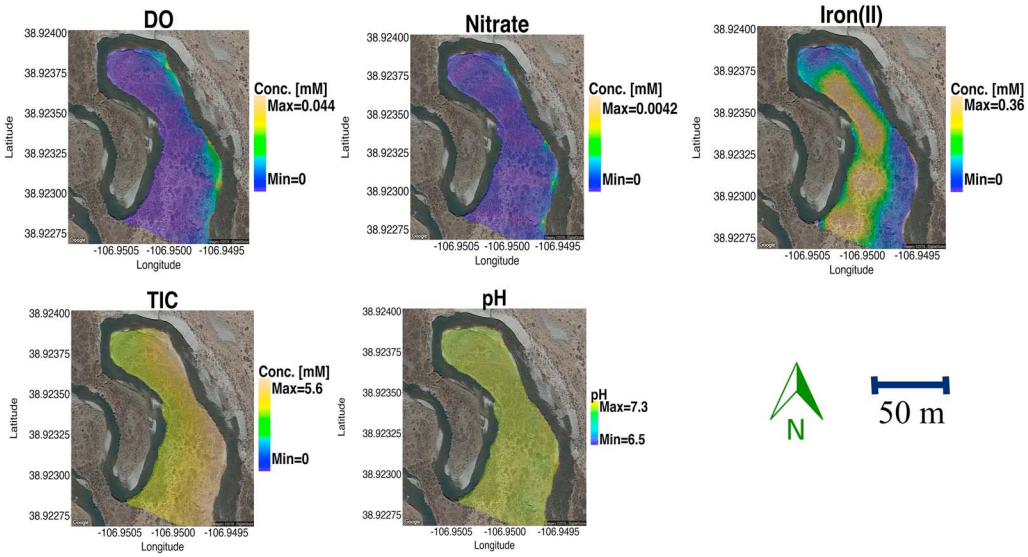

Figure 9. Computed spatial distributions of dissolved geochemical species in groundwater in the meander C.

that the concentrations of iron and TIC decreased along the flow paths close to the point bar. This behavior can be attributed to shorter residence times (due to smaller lengths of *T* transects; for example, T5) within the intrameander region close to the point bar, resulting in the greater availability of oxygen and a decline in the potential of reductive decomposition from other TEAs.

Together, these results indicate that the hyporheic intrameander domain can be divided into anoxic and suboxic zones. The suboxic classification indicates low O_2 conditions and NO_3^- reduction. The anoxic designation corresponds to Fe^{3+} reduction. This biogeochemical zonation is depicted in Figure 3, which shows that the suboxic zone was localized at both ends of the intrameander region.

4.3. Influence of Transient Conditions on Hyporheic Zone Processes

One of the goals of this paper was to understand how transient hydrologic conditions impact hyporheic exchange and biogeochemical processes in the subsurface. Therefore, here we describe the impact of river stage variations and rain events on redox zonation along the modeled transect.

4.3.1. Redox Zonation Driven by River Stage Variations

In this section, we show how river stage variations influenced the geochemical system using daily outputs of the model. Figure 10 shows how pH and the concentrations of various geochemical species such as DO, nitrate, iron, and TIC (*x* axis) responded to river stage fluctuations along the MCP transect using the baseline simulation. The *y* axis displays the time ranging from 23 October 2015 to 22 October 2016. The results show that high river stages (particularly, from mid-April to mid-June) promoted an increase in DO and nitrate because of the higher groundwater velocities (Figure 7). However, these geochemical species were entirely reduced within the first few meters of the transect. In contrast, iron, and TIC decreased near MCP1 during high-water conditions. Although oxygen-rich river water stimulates high microbial activity and would be expected to increase TIC, an effective decrease in TIC was obtained with high-water conditions because of river water intrusion, which was low in HCO_3^- (see, supporting information Table S7). In addition, the oxic water infiltration led to a decline in iron concentration near MCP1 during high-water conditions. Irrespective of water table fluctuations, the pH did not change appreciably over seasonal or annual time scales because of the effects of calcite mineral buffering the system's pH. Figure 10 also shows that redox gradients were relatively stable and unresponsive to minor water-level fluctuations during low-water conditions (mid-September to March). High iron concentrations near MCP1 indicated that low-water conditions promoted reducing conditions. In general, Figure 10 demonstrates that suboxic zones (near MCP1 and MCP5) showed more variability than the anoxic zone in response to transient hydrologic conditions.

It is evident that groundwater velocities resulting from river stage fluctuations control the redox zonation along the MCP transect over seasonal time scales (Figure 10). However, to better understand the influence

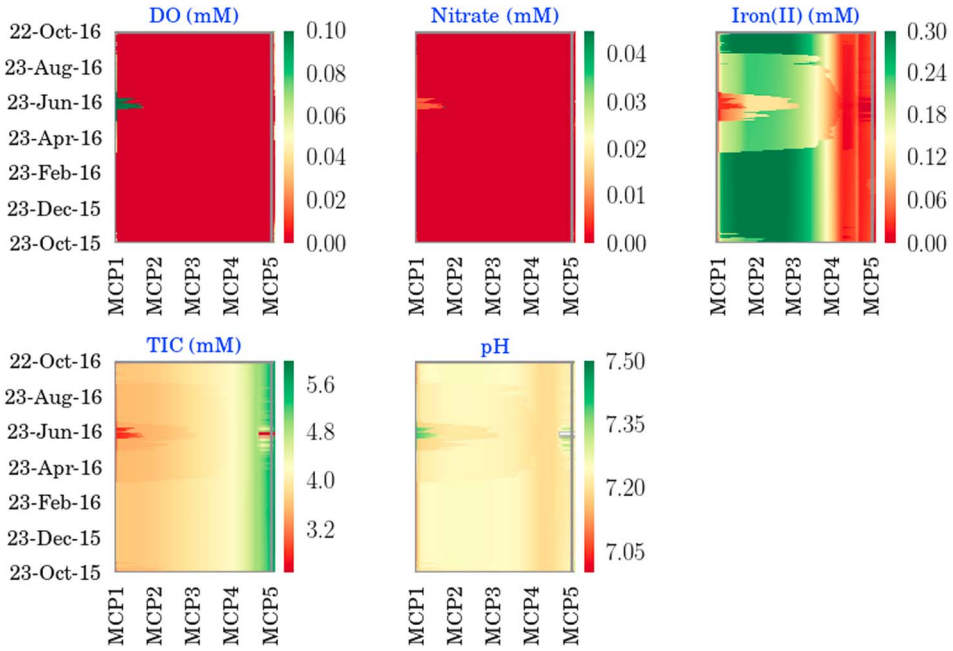

Figure 10. Simulated pH and geochemical species concentrations along the MCP transect (shown for different dates and locations as color maps) demonstrate that redox zonation is highly dynamic and respond to river stage fluctuations. The highest river stage at this site occurred in mid-April to June and then decreased until October.

of the hydraulic head gradients on redox fronts, we compared the baseline simulation (Figure 10) with simulations M1, M2, M3, and M4 (described in Table 1).

Simulation M1 imposed steady state river stages along the western (mean of the western river stage) and eastern (mean of the eastern river stage) boundaries. M1 produced a typical redox zonation along the MCP transect (see supporting information Figure S2), where dissolved oxygen and nitrate decreased, while iron and TIC concentrations increased along the intrameander flow paths. However, iron was low at MCP4 because of the oxic recharge from the gully.

Simulation M2 imposed transient river stages along the western boundary (same as the baseline simulation) and the eastern boundary, showing a constant stream gradient (~ − 0.20 m/m) over time. In other words, the eastern and western model boundaries demonstrated identical fluctuations in time. M2 showed relatively minor differences in pH and geochemical species compared to the baseline scenario (not shown here), thus indicating that redox zonation was primarily influenced by groundwater flux resulting from the river stage variations along the MCP transect.

Simulations M3 and M4 imposed transient river stages on the western and eastern boundaries, with 15% and 30% lower hydraulic gradients, respectively, than the baseline scenario. In other words, M4 had the lowest stream gradients among M3, M4, and the baseline scenario. M3 and M4 showed relatively modest differences from the baseline scenario in pH and geochemical species along the MCP transect. In addition, M3 and M4 manifested proportional changes in pH and other geochemical species in time. Therefore, for simplicity, here we present the differences between M4 and the baseline scenarios along the MCP transect resulting from river stage fluctuation (Figure 11). Figure 11 shows the percent difference in pH and various geochemical species (*x* axis) in M4 and the baseline simulation along the MCP transect resulting from river stage fluctuations, with reference values of unit pH and unit mM for geochemical species, respectively. The *y* axis displays the time from 23 October 2015 to 22 October 2016. Based on the results, DO and nitrate did not show any differences near MCP1. Although smaller groundwater velocities resulted in lower predicted DO and nitrate concentrations near MCP1, DO and nitrate were entirely consumed within the first few meters in the M4 and baseline scenarios. Hence, DO and nitrate did not appear to be visibly different in either case. Unlike the baseline scenario, DO was found to be slightly higher at MCP5 because of the less steep hydraulic gradients imposed in the M4 scenario. As expected, the resulting flow rate became relatively smaller and

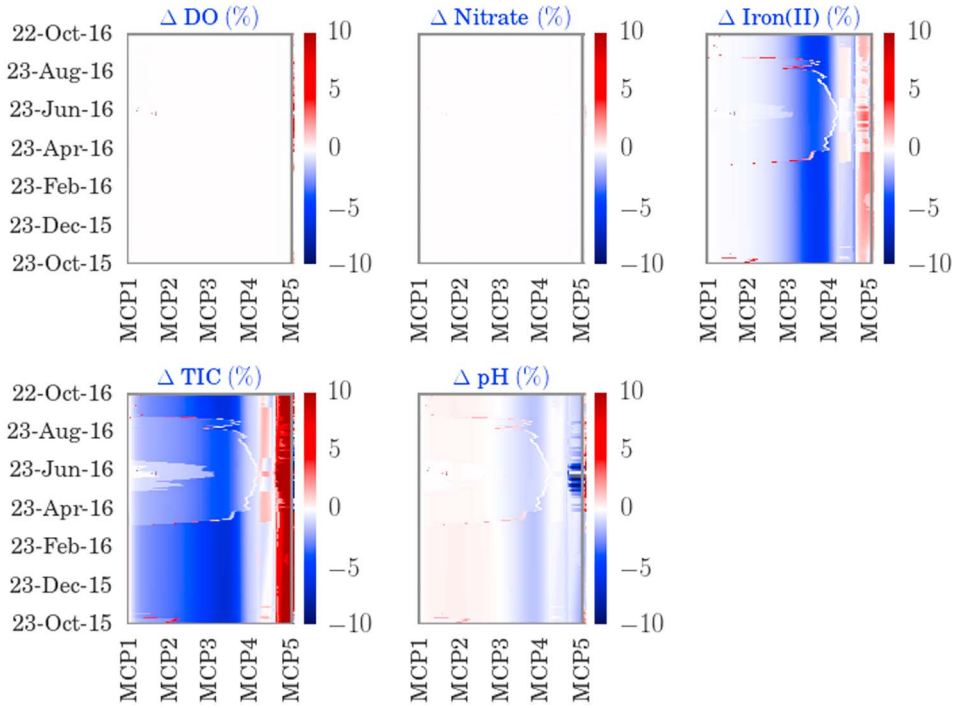

Figure 11. Percent difference in geochemical species concentrations and pH between the results of simulation M4 and the baseline scenario (positive if higher in the simulation M4).

flow directions occasionally reversed in the M4 simulation (see Figure 7 in July); therefore, the higher concentrations of DO were seen at MCP5. Nevertheless, no difference was shown in nitrate near MCP5 because the river water was low in nitrate. Iron showed no considerable difference from MCP1 to MCP3 (<3%) in M4 as compared to the baseline scenario, although iron was moderately lower near the gully (~6%). In addition, iron was slightly higher near MCP5 (~5%). The higher concentration of iron is due to the relatively smaller flow rate that allowed ample time for the biogeochemical reactions to occur even within this short distance. TIC showed slightly lower concentrations in M4 than the baseline scenario from MCP1 to MCP4. Lower groundwater velocities promoted lower DO and nitrate in the M4 simulation, which lowered the microbial activity. As a result, low microbial activity decreased TIC concentrations in the M4 simulation. However, the TIC concentration was significantly higher near MCP5 (~10%), which can be attributed to higher microbial activity resulting from higher DO and the longer residence time due to a smaller flow rate, thereby allowing ample time for biotic reactions to occur and produce TIC. Similarly, near MCP5, higher microbial activity slightly decreased the pH of the system; however, pH did not show any significant difference between MCP1 to MCP4 in M4 as compared to the baseline scenario.

4.3.2. Redox Zonation Driven by Rain Events

We describe observations from July—before rain and after one modest rain event totaling approximately 10 mm—and in the last week of August, during intermittent rain events totaling approximately 18 mm. Figure 12 presents the observations of EC and ORP (measured in millivolts) along the MCP transect. ORP is another method of estimating water's *bulk* redox condition (i.e., general tendency to gain or lose electrons). Although ORP is useful for tracking bulk redox changes, it cannot differentiate the potentials of specific redox couples and, thus, has practical limitations. Nevertheless, in our case, ORP showed that reducing conditions prevailed at MCP wells, although a small rainfall event in July did not significantly change the redox state of the intrameander pore water. Figure 8 also highlights that redox conditions did not show a significant response following a rain event in July at MCP wells. However, ORP showed a slight decline in August compared to July, indicating more reducing conditions at wells located in suboxic zones, such as MCP1, MCP2, and MCP5. Moreover, there was slightly higher Fe^{2+} and TIC at wells MCP2 and MCP3 in August compared to July, indicating higher microbial activity. Because only suboxic wells had lower ORP in August compared

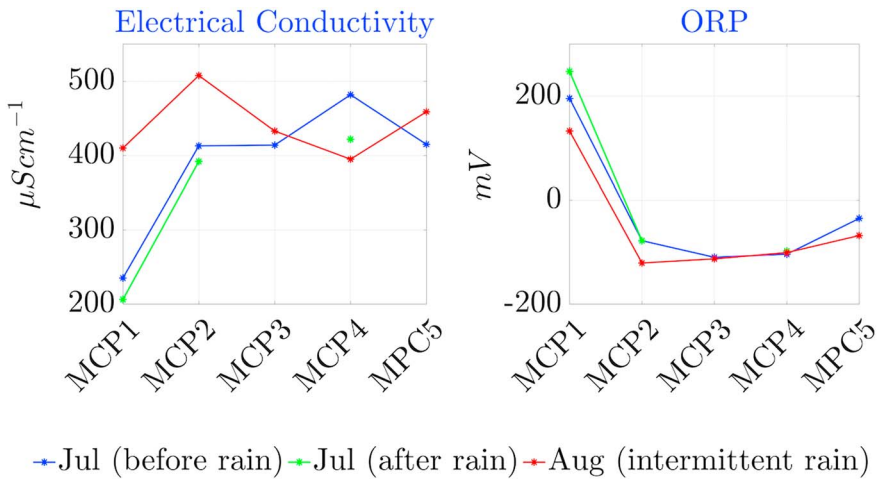

Figure 12. Measured electrical conductivity and ORP values along the MCP transect demonstrate how redox conditions change following rain events.

to July, redox conditions seem to be related to the residence time of groundwater along the MCP transect rather than to rainfall events, as the rain event would potentially alter redox conditions at each well. To further the argument, higher TIC values at wells MCP2 and MCP3 could result from either aerobic respiration or iron reduction—or both; however, higher TIC values along with slightly higher Fe^{2+} (resulting from slower biotic reactions) at well MCP3 suggest that redox conditions at MCP3 were more closely associated with the residence time of groundwater than to rainfall events. Still, other state variables (e.g., EC) moderately responded to intermittent rain events along the MCP transect. For example, EC did not change significantly at MCP wells in July following a minor rain event, although EC significantly increased at wells MCP1 and MCP2 following intermittent rain events in August. Although EC seems to change following intermittent rain events, more observations are required to corroborate our interpretation. These observations suggest that a small rain event does not influence redox conditions immediately, particularly in the anoxic zones. In conclusion, redox conditions appear to be related more to the residence time of groundwater along the MCP transect than to rainfall events.

5. Sensitivity Analysis

To characterize the impact of permeability and redox processes on biogeochemical transformation and microbial respiration in the hyporheic zone, we analyzed the sensitivity of predicted DO, nitrate, Fe^{2+} reduction, TIC, and pH profiles to permeability, mineral properties, and different biotic and abiotic reaction pathways along the MCP transect. In particular, we compared simulations M5 to M8 with the baseline scenario in July (due to availability of observations) to understand the influence of permeability and reaction pathways as follows.

5.1. Permeability Variations

We increased (M5 simulation) and decreased (M6 simulation) permeability by an order of magnitude for all stratigraphic layers (Table S2) to assess controls on biogeochemical transformation and microbial respiration along the modeled transect. Figure 13 demonstrates that Fe^{3+} reduction varied quite significantly across the permeability range, with the lower permeability scenario contributing to higher Fe^{2+} concentration in the groundwater. In contrast, lower Fe^{2+} concentration in conjunction with higher DO and nitrate values were predicted near wells MCP1 and MCP2 with the higher permeability scenario. In addition, Figure 13 shows that pH and TIC did not show significant variations with changes in permeability values. This was because soils with lower permeability values retarded hydrologic flow and reduced infiltration of DO and nitrate. However, an increase in residence time led to a nearly total consumption of DO and nitrate, inducing reducing conditions that favor microbial activity and Fe^{3+} reduction. Therefore, permeability exerted a major influence on Fe^{3+} reduction and a moderate effect on TIC. In addition, permeability had little impact on pH, which

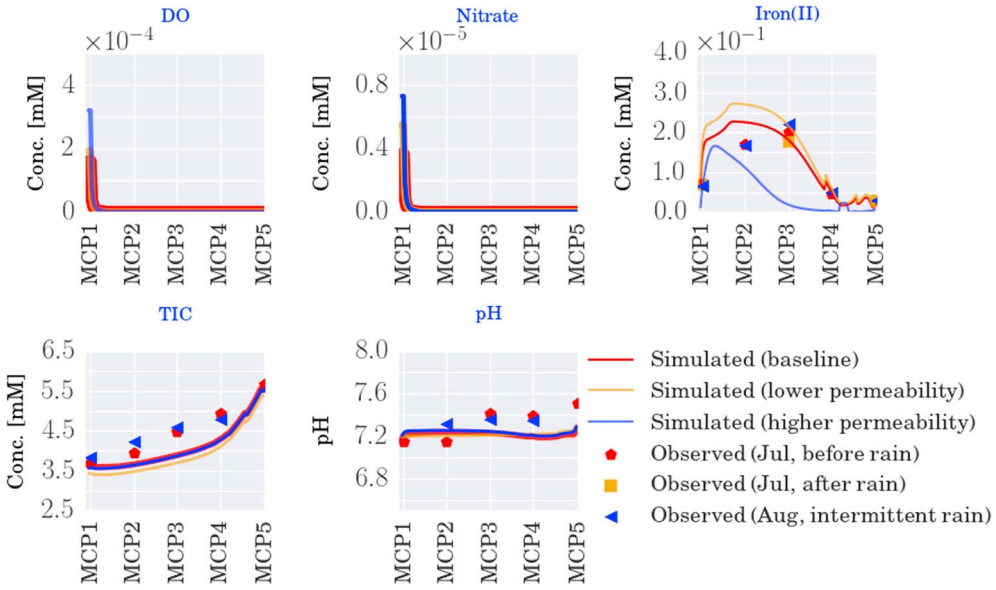

Figure 13. Effect of permeability on biogeochemical transformation and microbial respiration.

was predominantly controlled by the thermodynamic equilibrium of the carbonate system. Although an increase in residence time should result in higher microbial activity that effectively lowers pH, the presence of calcite mineral buffered the pH of the system.

We also compared the predicted pH and dissolved geochemical species using low and high permeability values with the baseline scenario for other times as well. The simulation results indicated that the higher permeability scenario typically promoted higher DO and nitrate, but lower Fe^{2+}, TIC, and pH in the groundwater and vice versa for the lower permeability scenario compared to the baseline scenario (not shown here). Yet for both permeability scenarios, any discernible changes in redox conditions were noticed primarily in the suboxic zones across low- and high-water conditions. Further, the corresponding variations in pH and geochemical species—due to low versus high permeability values—were more than ±10% in the suboxic zones whereas these variations were less than ±5% in the anoxic zones across different water conditions. In the high permeability scenario, for example, Fe^{2+} was 10% higher in the suboxic zone, whereas this change was only 4% in the anoxic zone for low-water compared to high-water conditions, respectively. Therefore, as would be expected, model results show the strong impact of permeability on water flow rates and thus residence times, affecting the redox gradients that develop within the hyporheic zone.

5.2. Relative Contribution of Reaction Pathways

To isolate and quantify the relative contributions of abiotic (M7 simulation), biotic (baseline simulation, which includes both heterotrophs and chemolithoautotrophs), and chemolithoautotrophic (M8 simulation) pathways on biogeochemical processing within the hyporheic zone, we analyzed the baseline, M7, and M8 simulations. These simulations (particularly, M7 and M8) were set up to quantify the relative contribution of mineral reactions especially pyrite oxidation, which is known to favor the removal of carbon, lowering of pH, and accumulation of iron oxides (Brantley et al., 2013; Jaffe et al., 2002; Jin et al., 2013; Wildman et al., 2004). Moreover, while chemolithoautotrophic activity is recognized to be an important pathway involving iron and sulfur cycling (Jewell et al., 2016), it is not known how various microbial pathways affect biogeochemical transformations under transient conditions in the hyporheic zone.

Figure 14 shows how DO, nitrate, Fe^{2+}, and TIC concentrations, as well as pH, responded along the MCP transect for these scenarios. As expected, pH did not change significantly across the scenarios because of carbonate buffering, while TIC varied moderately. DO and nitrate showed notable variability across these scenarios only at MCP1 and were completely consumed within the suboxic zone past well MCP1. Furthermore, Fe^{2+} varied significantly across these scenarios. The baseline scenario considering microbial contributions from

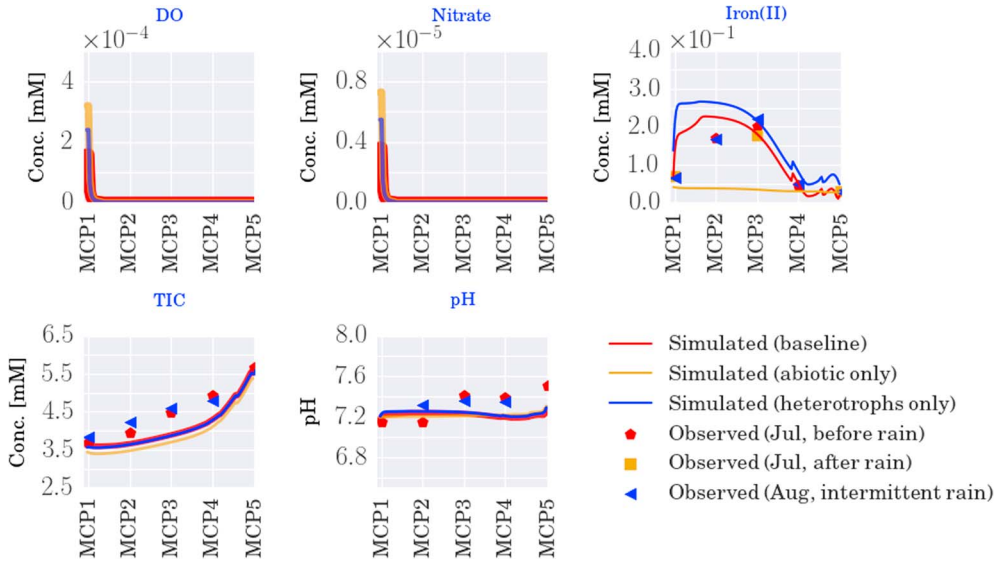

Figure 14. Effect of reaction pathways on biogeochemical transformation and microbial respiration.

both heterotrophic and chemolithoautotrophic pathways predicted lower levels of Fe^{2+} in the hyporheic system because chemolithoautotrophic pathways incorporated iron and sulfur cycling, thereby resulting in lower available Fe^{2+} concentration in groundwater. Model simulations suggest that approximately 18% of Fe^{2+} levels were contributed by abiotic reactions primarily due to the reduction of ferrihydrite, while chemolithoautotrophic pathways lowered Fe^{2+} levels by 34%.

We also compared the predicted pH and dissolved geochemical species from simulations M7 and M8 with the baseline scenario for other times as well (not shown here). The simulations results indicate that DO, nitrate, and pH were slightly higher during high-water conditions compared to low-water conditions in the suboxic zone for M7 (abiotic scenario). Anoxic zones did not show any significant variability in DO, nitrate, and pH for M7. In addition, Fe^{2+} and TIC did not change across different water conditions in both suboxic and anoxic zones. Higher DO, nitrate, and pH in the suboxic zone resulted from oxic water infiltration through high groundwater velocities as a consequence of the high river stage. Nevertheless, relatively short-term high groundwater velocities may limit their influence to suboxic zones alone. Because M7 did not include any biotic reactions, Fe^{2+} and TIC did not show any significant difference for low- or high-water conditions.

M8 simulation results indicate that DO and nitrate were identical in the groundwater for low- or high-water conditions. Because both the baseline and M8 included heterotrophs, DO and nitrate were no different in these scenarios. Although iron and pH were slightly higher while TIC was moderately lower in M8, these species did not manifest any corresponding variations in M8 compared to the baseline scenario for high or low-water conditions. Overall, we can conclude that the various pathways and the presence of minerals in the hyporheic zone significantly impact the biogeochemical transformation of iron and TIC, as would be expected. However, permeability has a greater impact compared to the tested reaction pathways for transient hydrologic conditions.

6. Contribution of a Single Meander to River Chemistry

Here we focus on the cumulative export of carbon (both inorganic and organic) and iron from a single meander to the river. For this purpose, we quantified the overall contribution of a meander to the river by integrating geochemical out-fluxes along the outside of a meander's bend using 2-D simulations of the *T* transects, as described in section 3.1. We performed these simulations for an entire year to capture the cumulative effect of water table fluctuations on the subsurface exports. We computed the net subsurface exports as a three-step process: first, computing the product of the groundwater flow velocity and concentration at the upgradient and downgradient model boundaries for each transect; second, computing the difference between

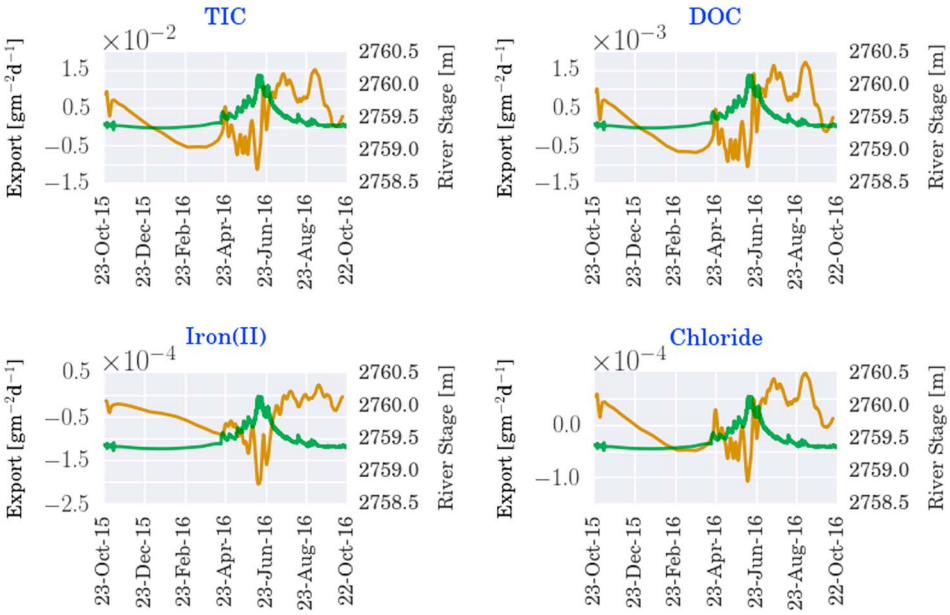

Figure 15. Net cumulative geochemical export of TIC, DOC, and iron (II) from a single meander. River stage is shown in green on the right *y* axis, whereas the net export is shown in golden color on the left *y* axis.

upgradient and downgradient fluxes; and third, integrating the difference between these volumetric fluxes and taking the areal average along the meander bend. It is worth mentioning that net exports are driven by hydrological transport as well as the availability of geochemical species (Dwivedi et al., 2018; Guan et al., 2011). Geochemical availability depends on the addition or removal of chemicals by groundwater flux or chemical transformation resulting from various reactions such as redox reactions. We computed the net export of TIC, DOC, iron, and chloride from a single meander to the river. While TIC, DOC, and iron participate in redox reactions, chloride is a conservative tracer and does not react with any chemical species; therefore, it can be used to inform transport-dominated (influenced by groundwater flux) processes. Accordingly, we compared exports of carbon and iron with chloride to ascertain contributions of redox processes on the net exports of these species.

Figure 15 shows the net export of TIC, DOC, iron, and chloride from a single meander to the river over time. The net exports and river stage variations are shown on the left *y* axis and the right *y* axis, respectively. Figure 15 indicates that subsurface exports varied considerably, particularly due to transient hydrologic conditions. Moreover, the net exports of different geochemical species tended to increase during the falling limb of the hydrograph. In fact, a single meander acted as a sink (net export < 0) for TIC, DOC, iron, and chlorides during the baseflow as well as high-water conditions. However, the meander gradually released these geochemical species into the river system during the falling limb. The meander acted as a sink during the high-water conditions because the river did not gain water from the subsurface during high-water conditions. To further this argument, Figures 7b and 7c demonstrate that, during high-water conditions, outfluxes were smaller than groundwater influxes. In contrast, during baseflow conditions, the fall of the water table brought less water to flow within the gravel layer, which resulted in low microbial activity and led to lower concentrations of TIC, DOC, and iron. Therefore, the meander acted as a sink during the extended baseflow conditions (also see Figure S3).

Figure 15 also shows that inorganic carbon exports were approximately 8 to 10 times greater than organic carbon exports to the river, whereas iron exports were relatively small. Although subsurface exports were primarily transport-dominated, microbial processes produced TIC and iron during low-water conditions that were eventually released to the river. Therefore, we conclude that the net exports of iron and carbon depend upon intermittent oxic and reductive conditions resulting from the episodic low- and high-water conditions. Overall, these simulations demonstrated how the complex coupling of processes control the net export of carbon and iron to the river system.

7. Caveats and Future Model Development

Previous studies have demonstrated that morphological characteristics of the meander, including sinuosity and topography, can change the residence time of geochemical species in the hyporheic zone, although mostly under steady state conditions (Boano et al., 2010; Brosofske et al., 1997; Naiman & Decamps, 1997; Schindler & Krabbenhoft, 1998; Stonedahl et al., 2010; Tonina & Buffington, 2007; Zarnetske et al., 2011). Here we evaluated how transient hydrological conditions influenced the lateral redox zonation within an intrameander region of the East River in Colorado. Consistent with the findings of previous studies, we demonstrated that permeability and hydraulic gradients impact the residence time of geochemical species, thereby exerting significant control over lateral redox zonation. Furthermore, this study advances our understanding of redox gradients and their controls under transient hydrological conditions. Accordingly, we showed that redox gradients were highly dynamic, and transient hydrologic conditions (e.g., changes in hydraulic gradients) and vertical hydrostratigraphy together had a substantial influence on the lateral redox zonation. In their study, Boano et al. (2010) showed that biogeochemical potential for the degradation of organic carbon is spatially variable because of spatially varying residence times within a meander. Here we demonstrated how reductive potential for multiple redox species declines from the neck to point bar of a meander. In addition, this study also highlighted the outsized impacts of microtopographic features such as gullies on redox processes.

Our study indicated that lateral redox gradients were primarily controlled by river stage fluctuations as temporal patterns of river chemistry did not vary significantly during low-water conditions (July and August). However, we did not have observations of river chemistry during the baseflow and high-water conditions. Therefore, we did not consider transient river chemistry in the current analysis, although we acknowledge that temporal patterns of river chemistry may cause uncertainty in our model results; future work will address these shortcomings. Nevertheless, this study is generic and provides valuable insights into biogeochemical processes resulting from transient conditions induced by the river stage and groundwater variations.

The model introduced here represented a two-dimensional intrameander region, but terrestrial ecosystems are spatially heterogeneous and include various subsystems, such as hill slopes and floodplains that may affect redox processes as well as coupled carbon and nitrogen cycling at large scales. Therefore, to bridge gaps between meander-, floodplain-, and watershed-modeling, three-dimensional representation with multiscale approaches will be required to account for impacts of morphological characteristics of the meander, including microtopography at the large scale. Developing a predictive understanding of biogeochemical processes and informing the level of complexity needed at the large scale are tasks we leave for future research.

8. Conclusions

The biogeochemical processes affecting redox zonation within the intrameander hyporheic zone of a high elevation mountainous catchment were evaluated using a 2-D variably saturated flow and reactive transport model, with the application of the numerical code PFLOTRAN. Model simulations incorporating microbial processes, mineral reactions, and transient flow processes produced realistic spatially resolved estimates of geochemical species, including DO, nitrate, iron (Fe^{2+}), TIC, and pH. The simulation results, consistent with observations, showed that nitrate and dissolved oxygen values decreased while Fe^{2+} values increased along the meander centerline away from the stream. The intrameander hyporheic zone displayed distinct anoxic and suboxic zones, with the suboxic zones being localized along the sides of the MCP transect. In general, suboxic zones showed higher variability than the anoxic zone in response to transient hydrologic conditions. Low-water conditions promoted reducing conditions. In addition, redox zonation along the MCP transect was highly dynamic and predominantly driven by groundwater velocities resulting from river stage fluctuations. We also found that microtopographic features such as gullies have a considerable influence on redox processes in the hyporheic zone.

Using sensitivity analyses, we found that permeability values were inversely related to the reductive potential in the hyporheic zone. In addition, the complex interactions of various abiotic and biotic pathways in the hyporheic zone exerted significant control on the biogeochemical transformation of iron and TIC. However, permeability had a greater influence on biogeochemical zonation compared to the reaction

pathways for transient hydrologic conditions. This study highlighted how transient hydrological conditions control the lateral redox zonation within the intrameander hyporheic zone. We further found that exports of carbon and iron were primarily transport driven, yet depended upon intermittent oxic and reductive conditions resulting from episodic low- and high-water conditions. In addition, the net exports of different geochemical species tended to increase as the river stage decreased. The findings of this study demonstrate the importance of including hydrologic transients, using a modern reactive transport approach, to quantify exports within the intrameander hyporheic zone at the riverine scale.

Acknowledgments
This material is based upon work supported by the Watershed Function Scientific Focus Area and Interoperable Design of Extreme-scale Application Software (IDEAS) at Lawrence Berkeley National Laboratory funded by the U.S. Department of Energy, Office of Science, Office of Biological and Environmental Research under award DE-AC02-05CH11231. This research used resources of the National Energy Research Scientific Computing Center, which is supported by the Office of Science of the U.S. Department of Energy under contract DE-AC02-05CH11231. The data used are listed in the references, tables, and supporting information. The authors thank Helen F. Malenda from Colorado School of Mines for her valuable suggestions, which greatly improved this manuscript.

References

Arora, B., Dwivedi, D., Hubbard, S. S., Steefel, C. I., & Williams, K. H. (2016). Identifying geochemical hot moments and their controls on a contaminated river floodplain system using wavelet and entropy approaches. *Environmental Modelling and Software*, *85*, 27–41. https://doi.org/10.1016/j.envsoft.2016.08.005

Arora, B., Mohanty, B. P., McGuire, J. T., & Cozzarelli, I. M. (2013). Temporal dynamics of biogeochemical processes at the Norman landfill site. *Water Resources Research*, *49*, 6909–6926. https://doi.org/10.1002/wrcr.20484

Arora, B., Spycher, N. F., Steefel, C. I., Molins, S., Bill, M., Conrad, M. E., et al. (2016). Influence of hydrological, biogeochemical and temperature transients on subsurface carbon fluxes in a flood plain environment. *Biogeochemistry*, *127*(2–3), 367–396. https://doi.org/10.1007/s10533-016-0186-8

Bardini, L., Boano, F., Cardenas, M. B., Revelli, R., & Ridolfi, L. (2012). Nutrient cycling in bedform induced hyporheic zones. *Geochimica et Cosmochimica Acta*, *84*, 47–61. https://doi.org/10.1016/j.gca.2012.01.025

Bear, J. (1972). Dynamics of fluids in porous media. *Soil Science*, *120*(2), 162–163. https://doi.org/10.1097/00010694-197508000-00022

Boano, F., Camporeale, C., Revelli, R., & Ridolfi, L. (2006). Sinuosity-driven hyporheic exchange in meandering rivers. *Geophysical Research Letters*, *33*, L18406. https://doi.org/10.1029/2006GL027630

Boano, F., Demaria, A., Revelli, R., & Ridolfi, L. (2010). Biogeochemical zonation due to intrameander hyporheic flow. *Water Resources Research*, *46*, W02511. https://doi.org/10.1029/2008WR007583

Boano, F., Revelli, R., & Ridolfi, L. (2008). Reduction of the hyporheic zone volume due to the stream-aquifer interaction. *Geophysical Research Letters*, *35*, L09401. https://doi.org/10.1029/2008GL033554

Brantley, S. L., Holleran, M. E., Jin, L., & Bazilevskaya, E. (2013). Probing deep weathering in the Shale Hills critical zone observatory, Pennsylvania (USA): The hypothesis of nested chemical reaction fronts in the subsurface. *Earth Surface Processes and Landforms*, *38*(11), 1280–1298. https://doi.org/10.1002/esp.3415

Briggs, M. A., Lautz, L. K., & Hare, D. K. (2014). Residence time control on hot moments of net nitrate production and uptake in the hyporheic zone. *Hydrological Processes*, *28*(11), 3741–3751. https://doi.org/10.1002/hyp.9921

Brosofske, K. D., Chen, J., Naiman, R. J., & Franklin, J. F. (1997). Harvesting effects on microclimatic gradients from small streams to uplands in western Washington. *Ecological Applications*, *7*(4), 1188–1200. https://doi.org/10.1890/1051-0761(1997)007[1188:HEOMGF]2.0.CO;2

Cardenas, M. B. (2007). Potential contribution of topography-driven regional groundwater flow to fractal stream chemistry: Residence time distribution analysis of Tóth flow. *Geophysical Research Letters*, *34*, L05403. https://doi.org/10.1029/2006GL029126

Cardenas, M. B. (2009). Stream-aquifer interactions and hyporheic exchange in gaining and losing sinuous streams. *Water Resources Research*, *45*, W06429. https://doi.org/10.1029/2008WR007651

Cozzarelli, I. M., Böhlke, J. K., Masoner, J., Breit, G. N., Lorah, M. M., Tuttle, M. L. W., & Jaeschke, J. B. (2011). Biogeochemical evolution of a landfill leachate plume, Norman, Oklahoma. *Ground Water*, *49*(5), 663–687. https://doi.org/10.1111/j.1745-6584.2010.00792.x

Davidson, E. A., Samanta, S., Caramori, S. S., & Savage, K. (2012). The dual Arrhenius and Michaelis-Menten kinetics model for decomposition of soil organic matter at hourly to seasonal time scales. *Global Change Biology*, *18*(1), 371–384. https://doi.org/10.1111/j.1365-2486.2011.02546.x

Doussan, C., Poitevin, G., Ledoux, E., & Delay, M. (1997). River bank filtration: Modelling of the changes in water chemistry with emphasis on nitrogen species. *Journal of Contaminant Hydrology*, *25*(1-2), 129–156. https://doi.org/10.1016/S0169-7722(96)00024-1

Dwivedi, D., Arora, B., Steefel, C. I., Dafflon, B., & Versteeg, R. (2018). Hot spots and hot moments of nitrogen in a riparian corridor. *Water Resources Research*, *54*, 205–222. https://doi.org/10.1002/2017WR022346

Dwivedi, D., & Mohanty, B. P. (2016). Hot spots and persistence of nitrate in aquifers across scales. *Entropy*, *18*(1), 25. https://doi.org/10.3390/e18010025

Dwivedi, D., Mohanty, B. P., & Lesikar, B. J. (2016). Impact of the linked surface water-soil water-groundwater system on transport of *E. coli* in the Subsurface. *Water, Air, & Soil Pollution*, *227*, 351. https://doi.org/10.1007/s11270-016-3053-2

Dwivedi, D., Steefel, I. C., Arora, B., & Bisht, G. (2017). Impact of intra-meander hyporheic flow on nitrogen cycling. *Procedia Earth and Planetary Science*, *17*, 404–407. https://doi.org/10.1016/j.proeps.2016.12.102

Gaskill, D. L., Mutschler, F. E., Kramer, J. H., Thomas, J. A., & Zahony, S. G. (1991). Geologic map of the gothic quadrangle, Gunnison County, Colorado, geologic quadrangle map GQ-1689. Washington, DC: U.S. Geol. Surv.

Gomez, J. D., Wilson, J. L., & Cardenas, M. B. (2012). Residence time distributions in sinuosity-driven hyporheic zones and their biogeochemical effects. *Water Resources Research*, *48*, W09533. https://doi.org/10.1029/2012WR012180

Gu, C., Hornberger, G. M., Mills, A. L., Herman, J. S., & Flewelling, S. A. (2007). Nitrate reduction in streambed sediments: Effects of flow and biogeochemical kinetics. *Water Resources Research*, *43*, W12413. https://doi.org/10.1029/2007WR006027

Guan, K., Thompson, S. E., Harman, C. J., Basu, N. B., Rao, P. S. C., Sivapalan, M., et al. (2011). Spatiotemporal scaling of hydrological and agrochemical export dynamics in a tile-drained Midwestern watershed. *Water Resources Research*, *47*, W00J02. https://doi.org/10.1029/2010WR009997

Hammond, G. E., Lichtner, P. C., & Mills, R. T. (2014). Evaluating the performance of parallel subsurface simulators: An illustrative example with PFLOTRAN. *Water Resources Research*, *50*, 208–228. https://doi.org/10.1002/2012WR013483

Handley, K. M., VerBerkmoes, N. C., Steefel, C. I., Williams, K. H., Sharon, I., Miller, C. S., et al. (2013). Biostimulation induces syntrophic interactions that impact C, S and N cycling in a sediment microbial community. *The ISME Journal*, *7*(4), 800–816. https://doi.org/10.1038/ismej.2012.148

Harvey, J. W., & Fuller, C. C. (1998). Effect of enhanced manganese oxidation in the hyporheic zone on basin-scale geochemical mass balance. *Water Resources Research*, *34*(4), 623–636. https://doi.org/10.1029/97WR03606

Helgeson, H. C., Delany, J. M., Nesbitt, H. W., & Bird, D. K. (1978). Summary and critique of the thermodynamic properties of rock-forming minerals. *American Journal of Science*, *278*, 1–229.

Hubbard, S. S., Williams, K. H., Agarwal, D., Banfield, J., Beller, H., Bouskill, N., et al. (2018). The East River, Colorado, Watershed: A mountainous community testbed for improving predictive understanding of multiscale hydrological– biogeochemical dynamics. *Vadose Zone Journal*, *17*, 180061. https://doi.org/10.2136/vzj2018.03.0061

Jaffe, L. A., Peucker-Ehrenbrink, B., & Petsch, S. T. (2002). Mobility of rhenium, platinum group elements and organic carbon during black shale weathering. *Earth and Planetary Science Letters*, *198*(3–4), 339–353. https://doi.org/10.1016/S0012-821X(02)00526-5

Jewell, T. N., Karaoz, U., Brodie, E. L., Williams, K. H., & Beller, H. R. (2016). Metatranscriptomic evidence of pervasive and diverse chemolithoautotrophy relevant to C, S, N and Fe cycling in a shallow alluvial aquifer. *ISME Journal*, *10*(9), 2106–2117. https://doi.org/10.1038/ismej.2016.25

Jin, L., Mathur, R., Rother, G., Cole, D., Bazilevskaya, E., Williams, J., et al. (2013). Evolution of porosity and geochemistry in Marcellus formation black shale during weathering. *Chemical Geology*, *356*, 50–63. https://doi.org/10.1016/j.chemgeo.2013.07.012

Kenwell, A., Navarre-Sitchler, A., Prugue, R., Spear, J. R., Hering, A. S., Maxwell, R. M., et al. (2016). Using geochemical indicators to distinguish high biogeochemical activity in floodplain soils and sediments. *Science of the Total Environment*, *563-564*, 386–395. https://doi.org/10.1016/j.scitotenv.2016.04.014

Knowles, R. (1982). Denitrification. *Microbiological Reviews*, *46*(1), 43–70. https://doi.org/10.1128/CMR.5.4.356.Updated

Li, L., Steefel, C. I., Kowalsky, M. B., Englert, A., & Hubbard, S. S. (2010). Effects of physical and geochemical heterogeneities on mineral transformation and biomass accumulation during biostimulation experiments at rifle, Colorado. *Journal of Contaminant Hydrology*, *112*(1–4), 45–63. https://doi.org/10.1016/j.jconhyd.2009.10.006

Loeppert, R. H., & Inskeep, W. P. (1996). Iron. In *Methods of soil analysis. Part 3. Chemical methods* (Vol. 23, pp. 639–664). Madison, Wisconsin: Soil Science Society of America, Inc. American Society of Agronomy, Inc.

Luther, G. W., Findlay, A. J., MacDonald, D. J., Owings, S. M., Hanson, T. E., Beinart, R. A., & Girguis, P. R. (2011). Thermodynamics and kinetics of sulfide oxidation by oxygen: A look at inorganically controlled reactions and biologically mediated processes in the environment. *Frontiers in Microbiology*, *2*. https://doi.org/10.3389/fmicb.2011.00062

Maggi, F., Gu, C., Riley, W. J., Hornberger, G. M., Venterea, R. T., Xu, T., et al. (2008). A mechanistic treatment of the dominant soil nitrogen cycling processes: Model development, testing, and application. *Journal of Geophysical Research*, *113*, G02016. https://doi.org/10.1029/2007JG000578

Majzlan, J., Navrotsky, A., & Schwertmann, U. (2004). Thermodynamics of iron oxides: Part III, Enthalpies of formation and stability of ferrihydrite (~Fe (OH)3/4(S04)1/8), and ε-Fe2O3. *Geochmica et Cosmochimica Acta*, *68*(5), 1049–1059.

Markstrom, S. L., Hay, L. E., Ward-Garrison, C. D., Risley, J. C., Battaglin, W. A., Bjerklie, D. M., et al. (2012). Integrated watershed-scale response to climate change for selected basins across the United States. U.S. Geological Survey Scientific Investigations Report 2011–5077, 143. Retrieved from http://pubs.usgs.gov/sir/2011/5077/

Marzadri, A., Tonina, D., Bellin, A., Vignoli, G., & Tubino, M. (2010). Semianalytical analysis of hyporheic flow induced by alternate bars. *Water Resources Research*, *46*, W07531. https://doi.org/10.1029/2009WR008285

Mayer, K. U., Alt-Epping, P., Jacques, D., Arora, B., & Steefel, C. I. (2015). Benchmark problems for reactive transport modeling of the generation and attenuation of acid rock drainage. *Computational Geosciences*. https://doi.org/10.1007/s10596-015-9476-9

Mayer, K. U., Frind, E. O., & Blowes, D. W. (2002). Multicomponent reactive transport modeling in variably saturated porous media using a generalized formulation for kinetically controlled reactions. *Water Resources Research*, *38*(9), 1174. https://doi.org/10.1029/2001WR000862

Morrison, S. J., Goodknight, C. S., Tigar, A. D., Bush, R. P., & Gil, A. (2012). Naturally occurring contamination in the Mancos shale. *Environmental Science and Technology*, *46*(3), 1379–1387. https://doi.org/10.1021/es203211z

Naiman, R. J., & Decamps, H. (1997). The ecology of interfaces: Riparian zones. *Annual Review of Ecology, Evolution, and Systematics*, *28*(1), 621–658. https://doi.org/10.1146/annurev.ecolsys.28.1.621

Palandri, J. L., & Kharaka, Y. K. (2004). A compilation of rate parameters of water-mineral interaction Kinetics for application to geochemical modeling.

Palmer, K., Drake, H. L., & Horn, M. A. (2010). Association of novel and highly diverse acid-tolerant denitrifiers with N_2O fluxes of an acidic fen. *Applied and Environmental Microbiology*, *76*(4), 1125–1134. https://doi.org/10.1128/AEM.02256-09

Palumbo-Roe, B., Wragg, J., & Banks, V. J. (2012). Lead mobilisation in the hyporheic zone and river bank sediments of a contaminated stream: Contribution to diffuse pollution. *Journal of Soils and Sediments*, *12*(10), 1633–1640. https://doi.org/10.1007/s11368-012-0552-7

Parkhurst, D. L., & Appelo, C. A. J. (1999). User's guide to PHREEQC (Version 2)—A computer program for speciation, batch-reaction, one-dimensional transport, and inverse geochemical calculations. Denver, CO.

Revelli, R., Boano, F., Camporeale, C., & Ridolfi, L. (2008). Intra-meander hyporheic flow in alluvial rivers. *Water Resources Research*, *44*, W12428. https://doi.org/10.1029/2008WR007081

Richards, L. A. (1931). Capillary conduction of liquids through porous mediums. *Journal of Applied Physics*, *1*(5), 318–333. https://doi.org/10.1063/1.1745010

Russell, E. W. (1973). *Soil Conditions and plant growth* (10th ed.). London: Longmans Publishing.

Schindler, J. E., & Krabbenhoft, D. P. (1998). The hyporheic zone as a source of dissolved organic carbon gases to a temperate forest stream. *Biogeochemistry*, *43*(2), 157–174. https://doi.org/10.1023/A:1006005311257

Shock, E. L., Sassani, D. C., Willis, M., & Sverjensky, D. A. (1997). Inorganic species in geologic fluids: Correlations among standard molal thermodynamic properties of aqueous ions and hydroxide complexes. *Geochimica et Cosmochimica Acta*, *61*(5), 907–950. https://doi.org/10.1016/S0016-7037(96)00339-0

Siergieiev, D., Ehlert, L., Reimann, T., Lundberg, A., & Liedl, R. (2015). Modelling hyporheic processes for regulated rivers under transient hydrological and hydrogeological conditions. *Hydrology and Earth System Sciences*, *19*(1), 329–340. https://doi.org/10.5194/hess-19-329-2015

SNL (2007). *Qualification of thermodynamic data for geochemical modeling of mineral-water interactions in dilute systems. Las Vegas, Nevada*. Las Vegas, Nevada: Sandia National Laboratories.

Stonedahl, S. H., Harvey, J. W., Wörman, A., Salehin, M., & Packman, A. I. (2010). A multiscale model for integrating hyporheic exchange from ripples to meanders. *Water Resources Research*, *46*, W12539. https://doi.org/10.1029/2009WR008865

Tonina, D., & Buffington, J. M. (2007). Hyporheic exchange in gravel bed rivers with pool-riffle morphology: Laboratory experiments and three-dimensional modeling. *Water Resources Research*, *43*, W01421. https://doi.org/10.1029/2005WR004328

Wainwright, H., & Williams, K. H. (2017). LiDAR collection in August 2015 over the East River Watershed, Colorado, USA. https://doi.org/10.21952/WTR/1412542

Widdowson, M. A., Molz, F. J., & Benefield, L. D. (1988). A numerical transport model for oxygen- and nitrate-based respiration linked to substrate and nutrient availability in porous media. *Water Resources Research*, *24*(9), 1553–1565. https://doi.org/10.1029/WR024i009p01553

Wildman, R. A., Berner, R. A., Petsch, S. T., Bolton, E. W., Eckert, J. O., Mok, U., & Evans, J. B. (2004). The weathering of sedimentary organic matter as a control on atmospheric O-2: I. Analysis of a black shale. *American Journal of Science*, *304*(3), 234–249. https://doi.org/10.2475/ajs.304.3.234

Williamson, M. A., & Rimstidt, J. D. (1994). The kinetics and electrochemical rate-determining step of aqueous pyrite oxidation. *Geochimica et Cosmochimica Acta*, *58*(24), 5443–5454. https://doi.org/10.1016/0016-7037(94)90241-0

Winnick, M. J., Carroll, R. W. H., Williams, K. H., Maxwell, R. M., Dong, W., & Maher, K. (2017). Snowmelt controls on concentration-discharge relationships and the balance of oxidative and acid-base weathering fluxes in an alpine catchment, East River, Colorado. *Water Resources Research*, *53*, 2507–2523. https://doi.org/10.1002/2016WR019724

Wu, Y., Ajo-Franklin, J. B., Spycher, N., Hubbard, S. S., Zhang, G., Williams, K. H., et al. (2011). Geophysical monitoring and reactive transport modeling of ureolytically-driven calcium carbonate precipitation. *Geochemical Transactions*, *12*(1), 7. https://doi.org/10.1186/1467-4866-12-7

Yabusaki, S. B., Wilkins, M. J., Yilin, F., Williams, K. H., Arora, B., Bargar, J. R., et al. (2017). Water table dynamics and biogeochemical cycling in a shallow, variably-saturated floodplain (in review). *Environmental Science & Technology*, acs.est.6b04873. https://doi.org/10.1021/acs.est.6b04873

Zarnetske, J. P., Haggerty, R., Wondzell, S. M., & Baker, M. A. (2011). Dynamics of nitrate production and removal as a function of residence time in the hyporheic zone. *Journal of Geophysical Research*, *116*, G01025. https://doi.org/10.1029/2010JG001356